



# High precision real-time insertion device and monochromator synchronization at NSLS-II

D. Hidas<sup>\*</sup>, A.M. Kiss, M. Rakitin, J. Sinsheimer, T. Tanabe, M. Musardo

Brookhaven National Laboratory, Upton, NY 11973, USA

## ARTICLE INFO

### Keywords:

Insertion device  
Control system  
Spectrum  
Light source  
Fly scan  
Monochromator  
Synchronization  
Bluesky

## ABSTRACT

Insertion devices have become the dominant photon source at synchrotron and free electron laser light source facilities the world over. Undulators, characterized by their small deflection parameter, exhibit a high degree of constructive interference in photon production from high energy charged particle beams leading to very high photon rates at specific harmonics of the fundamental frequency with relatively narrow spectral widths. Spectroscopic measurements of interest typically span several of these harmonic widths, which requires precision adjustment of an undulator's magnetic gap to maintain peak flux within the much narrower bandwidth of a beamline monochromator at the desired energy. High precision insertion device controls are developed at NSLS-II including real-time linked control of monochromator hardware allowing for fast, high precision, hardware triggered, spectroscopic measurements. This fast fly scan method is described, compared statistically for self consistency, and shown to be far superior in both efficiency and accuracy as compared to standard step scan measurements.

## 1. Introduction

Many beamlines at today's synchrotron and free electron laser (FEL) facilities throughout the world have a keen interest in studying phenomena and materials by means of spectroscopic characterization of energy dependent interactions. Undulators have become commonplace in synchrotron and FEL sources due to the highly desirable effects of constructive interference that occur at odd multiples of the fundamental harmonic and strong suppression between peaks as can be seen in Fig. 1. Unlike their bending magnet and large deflection parameter ( $K$ ) wiggler broad spectrum counterparts, undulator radiation tends to be tightly collimated and the spectrum characterized by narrow spectral peaks. A typical spectroscopic measurement will span several of these spectral widths as illustrated in Fig. 2, requiring adjustment of the undulator field by means of changing the magnetic gap in order to maintain peak flux at the desired photon energy.

The relationship between spectral peaks and gap is both simulated with the OSCARS [1] software using magnetic measurement data for the 1.5 m long 21 mm period in-vacuum undulator (IVU21) [2] at the Sub-micron Resolution X-ray Spectroscopy (SRX) beamline at NSLS-II as well as measured at the beamline. Previous spectrum based undulator alignment has yielded spectra in agreement with simulation [3]. The current state of spectra and spectral peaks versus magnetic gap are compared in Fig. 3, are in good agreement with simulation, and are notably not characterized by a linear relationship.

In spectroscopic measurements it is necessary to take data over a range of photon energies and a standard baseline course is to independently position the undulator gap and monochromator for the desired energy and step through a series of such points stopping to collect data at each. This starting and stopping is costly in time and should be avoided where possible. A common mistake may be to assume that these static point measurements will yield a more precise result than data acquired from a system in motion, however the opposite is observed in fly scans developed for the SRX beamline.

Previous insertion device and monochromator synchronization techniques achieved some degree of synchronization and produced favorable results, however have been subject to control, network, or primary-secondary feedback related latencies [4]. The synchronous undulator-monochromator fly scan developed at NSLS-II for the SRX beamline is real-time coordinated high precision motion of all involved axes and hardware triggering with precise timing. There are no latencies related to motion, feedback, readbacks, controls, or readouts. Once a scan is started there is no intervention by an external computer or peripheral until a scan pass is finished when the acquired data is then collected.

## 2. Insertion device precision control

Beginning in 2018 nine insertion device control systems were re-worked in-situ to improve both their reliability and precision [5].

<sup>\*</sup> Corresponding author.

E-mail address: [dhidas@bnl.gov](mailto:dhidas@bnl.gov) (D. Hidas).

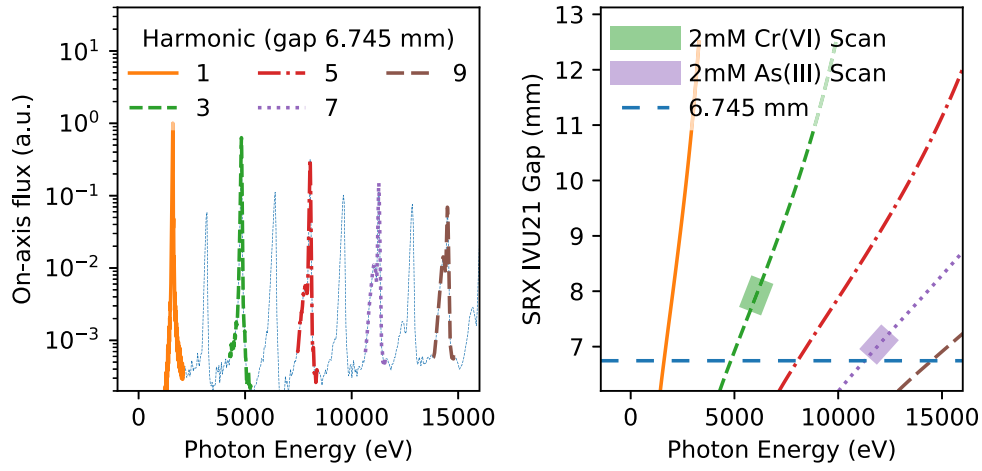


Fig. 1. Left: Multi-electron spectrum simulated for IVU21 at a gap of 6.745 mm resulting in an effective magnetic field of 0.89 T ( $K = 1.74$ ) with odd harmonics highlighted. Right: The SRX IVU21 magnetic gap as a function of photon energy for odd harmonics with the gap of 6.745 mm indicated by the horizontal dashed line which corresponds to the spectrum in the left plot.

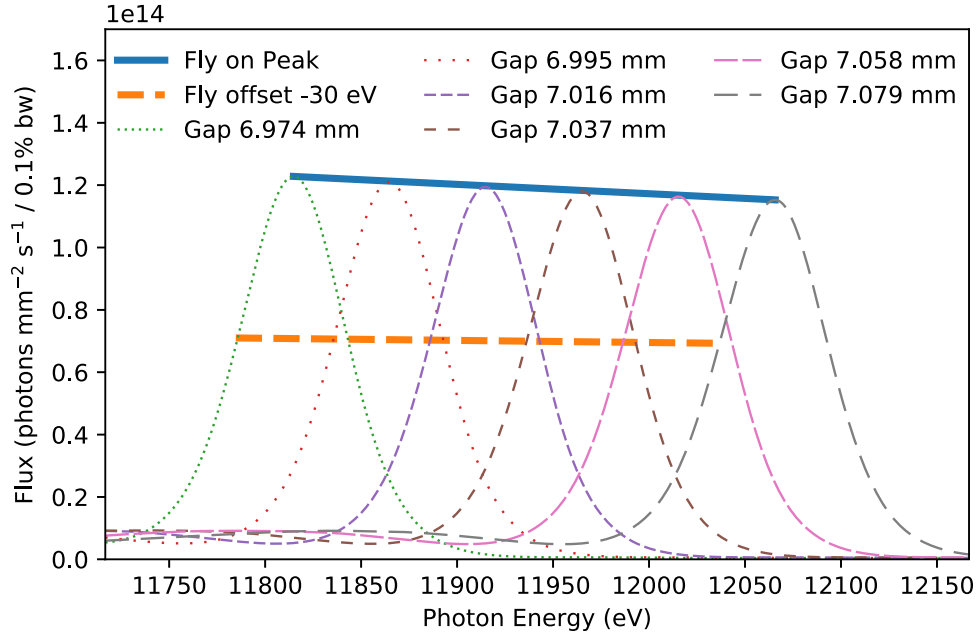


Fig. 2. Example fly scan compared to individual on-axis spectral peaks from multi-electron simulations taking into consideration the electron beam emittance, beta functions, and energy spread for IVU21 at stationary magnetic gaps. The full width at half maximum for spectral peaks in this energy range is 66 eV. It is possible to run fly scans on the peak or offset from the peak to reduce photon flux for sensitive samples.

Among these was the IVU21 for the SRX beamline. This device consists of 4 servo-driven axes (plus an additional one for coarse elevation adjustments not used herein) each having a 1 nm pitch absolute linear encoder and read-head mounted between the movable girder and stationary frame used for position feedback and rear motor-mounted rotary encoders used for velocity feedback. The 4 axes of interest are the top-upstream (TU), top-downstream (TD), bottom-upstream (BU), and bottom-downstream (BD) where upstream and downstream are in reference to the electron beam direction as installed. These axes are easily transformed to the more common coordinate system of gap, elevation, taper, and tilt according to Eq. (1).

$$\begin{bmatrix} \text{gap} \\ \text{elevation} \\ \text{taper} \\ \text{tilt} \end{bmatrix} = \begin{bmatrix} \frac{1}{2} & \frac{1}{2} & \frac{1}{2} & \frac{1}{2} \\ \frac{1}{4} & \frac{1}{4} & -\frac{1}{4} & -\frac{1}{4} \\ 1 & -1 & 1 & -1 \\ \frac{1}{2} & -\frac{1}{2} & -\frac{1}{2} & \frac{1}{2} \end{bmatrix} \begin{bmatrix} \text{TU} \\ \text{TD} \\ \text{BU} \\ \text{BD} \end{bmatrix} \quad (1)$$

The motion controller used is the Delta Tau Turbo PMAC2 Brick Controller which is driving these axes using external servo amplifiers by

means of a  $\pm 10$  V variable torque output signal. The servo amplifier and motor combination has an internal continually adjusting proportional, integral, and derivative (PID) gains with respect to the rotary encoder feedback which provides added stability and requires no tuning effort. The extended PID parameters in the Delta Tau are carefully tuned by hand using short moves at different gaps and adjusting as necessary to minimize following errors during motion as well as achieve reasonable acceleration performance. This is then verified over the full range of motion as magnetic forces can change dramatically as a function of gap. These axes are combined in a coordinate system on the controller and make use of forward and inverse kinematics. The inverse kinematics are defined by Eq. (1) while inverting the matrix in this equation provides the forward kinematic equations.

Once the optimal elevation, taper, and tilt are set they are kept constant for user operation. The gap is then changed to vary the energy of the resultant spectral peaks, thus precision control of this parameter is of crucial importance. Fig. 4 shows the combined gap following error over the entire range of motion for IVU21. This data is collected in real

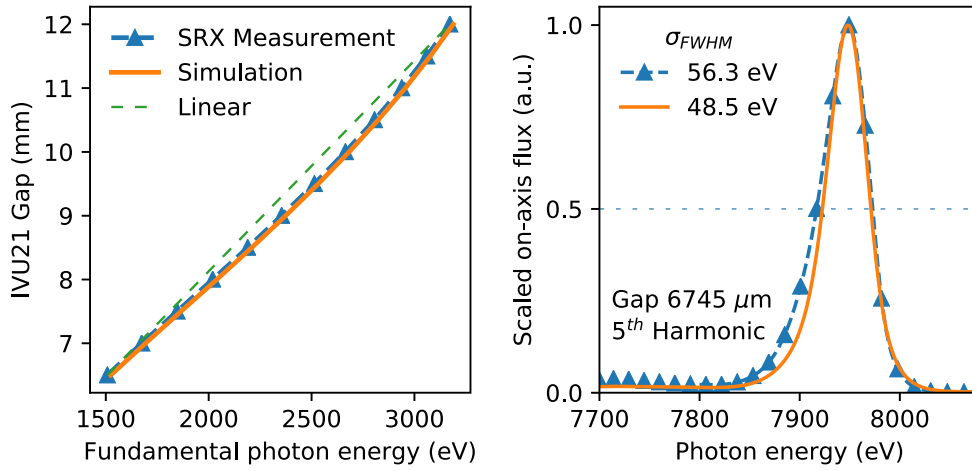


Fig. 3. Left: Gap as a function of energy curves for the first harmonic as calculated from magnetic measurements and simulation compared with beamline measurements. Right: Simulation compared to beamline measurements of the fifth harmonic spectral peak at a magnetic gap of 6.745 mm.

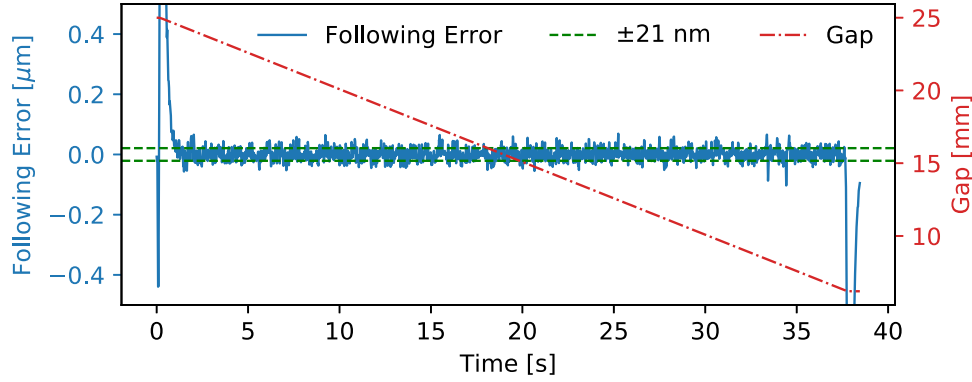


Fig. 4. Following error in the gap for IVU21 throughout the entire range of motion. The dashed lines indicate the following error RMS at  $\pm 21$  nm.

time using internal buffers within the controller and suffers no latency as the encoder readout rate is over 1 MHz and servo update cycle orders of magnitude lower at close to 2.4 kHz. The error in the gap position during motion excluding 0.5 s at the beginning and end of motion is shown to have a mean well below 1 nm with an RMS of 21 nm whereas previously gap repeatability was approximately 1  $\mu\text{m}$  and frequently the taper would exceed the 10  $\mu\text{m}$  threshold resulting in an error condition. When fly scanning the acceleration and deceleration phases are placed outside of any data collection windows.

### 3. SRX beamline

The SRX beamline is described in detail elsewhere [6]. The main components in the context of synchronization are the monochromator and detectors used during a scan. The Horizontal Double Crystal Monochromator (HDCM) of the SRX beamline is an in-vacuum silicon double crystal monochromator. There are a total of 8 motorized axes for precision adjustment, alignment, and focusing. The two crystals are both mounted on a common rotational stage which defines the common Bragg angle  $\theta$ . This common Bragg angle along with an axis for relative translation of the downstream crystal to provide a fixed exit position are the two axes primarily used to select the photon energy. Eqs. (2) and (3) describe the relationship of  $\theta$ , the downstream crystal translation ( $x_c$ ), and resultant photon energy  $E$  where  $h$  is Planck's constant,  $c$  the speed of light, and  $d_c$ ,  $X_{off}$ ,  $C_X$ ,  $C_T$ ,  $\Delta_\theta$ , are calibration constants relating to the crystal atomic spacing, a horizontal offset parameter, relative horizontal offset for the second crystal, second crystal perpendicular translation offset, and Bragg angle offset, which are determined from a fit of beamline spectroscopy measurements to

a known absorption edge. The value of these parameters are given in Table 1. For optimal transmittance at the specified energy  $\theta$  and  $x_c$  must be such that  $E(\theta) = E(x_c)$ .

$$E(\theta) = \frac{hc}{2d_c \sin(\theta + \Delta_\theta)} \quad (2)$$

$$E(x_c) = \frac{hc}{2d_c} \left[ 1 - \left( \frac{X_{off}}{2} \frac{1}{C_X - x_c + C_T} \right)^2 \right]^{-\frac{1}{2}} \quad (3)$$

The HDCM is controlled by a Delta Tau GeoBrick LV. In-vacuum stepper motors for the Bragg and translation axes are driven using the standard internal amplifiers with encoder feedback with a resolution corresponding to 0.13  $\mu\text{rad}$  and 0.05  $\mu\text{m}$  respectively. For independent HDCM use no forward and inverse kinematic routines are written in the controller. For step scanning or moving to specific energies this may not be necessary for many beamlines, but it will become essential for high precision fly scanning. It is noted that the translation motion ( $x_c$ ) relative to encoder resolution is small and would benefit from moving to a 1 nm scale.

Two detectors are currently used in fly scanning. One is an upstream ion chamber which provides a current proportional to the absolute incident photon flux. This current is converted to a voltage which is input into a voltage to frequency converter. The output pulses of this converter are counted in select windows by an SIS3801 VME (Versa Module Eurocard) Multi Channel Scaler where an advance signal, following the 5 V Transistor–Transistor Logic (TTL) standard, is used to differentiate time intervals of interest. A Vortex ME4 silicon drift detector is paired with a Quantum Detectors Xspress3 4-channel readout module for fluorescence measurements. Both of these detectors accept a standard TTL hardware trigger.

**Table 1**  
HDCM parameters and calibration coefficients.

Parameter	Value	Units
$hc$	12.3984	keV Å
$d_c$	3.128	Å
$C_X$	15.0347	mm
$C_T$	3.6	mm
$X_{off}$	24.770	mm
$\Delta_\theta$	0.2232	deg°

#### 4. Undulator and monochromator synchronization

The IVU21 and HDCM PMAC controllers are synchronized using the PMAC Motion and Control Ring Optical (MACRO) interface via a dedicated optical fiber link where the IVU21 controller serves as the ring primary controller and is used to coordinate motion during a fly scan. This link provides a 125 megabit per second data rate and servo update rates up to 65 kHz. This MACRO connection allows direct control of motors on the HDCM from the IVU21 controller with no latency and allows for their inclusion in the forward and inverse kinematic routines. The ring primary is used to close the position loop and sends torque commands to the HDCM controller while commutation is still performed by the HDCM controller. This fly scan mode may be enabled and disabled at will and assurances have been made such that accelerator control room requests will take precedence, automatically disabling this mode and function in their normal manner. When the fly scan mode is enabled both the Bragg and translation motor control are handed over to the IVU21 controller and all axis movement thereafter is performed by the IVU21 controller.

The handshake and pass-over of the two HDCM axes is initiated by a channel access (CA) [7] request in the accelerator network to the IVU21 Input/Output Controller (IOC) coming from the beamline through a CA gateway, which is then passed to the IVU21 controller by setting a basic internal variable. Each controller has an independent internal program (a software based PLC) running to coordinate this handshake. The PLC on the IVU21 controller sees the request first with the change of variable, copies all parameters for the remote motors over the MACRO link except for the PID related variables, then writes to a remote variable via the MACRO link which requests control of the 2 HDCM motors. When the request is received by the HDCM controller several internal checks are made and the motors are configured for remote control in torque control mode, and the HDCM controller updates its local variable with a success bit, or an error flag in case of failure. The IVU21 controller monitors the variable local to the HDCM and upon success will read the current position of the 2 HDCM remote motors, place the 4 local and 2 remote motors in the fly scan coordinate system using forward and inverse kinematics, and mark its own local variable for fly scan enabled signaling that it is complete and ready. The remote HDCM motor PID variables are determined from tuning on the IVU21 controller when the remote control is enabled.

At this point the IVU21 and HDCM act in unison and the axis of interest and use becomes energy ( $E$ ), whereas Gap,  $\theta$ , and  $x_c$  are no longer directly input by the user. The relationship of  $\theta$  and  $x_c$  to  $E$  are the invertible analytic expressions previously described. It is very important to note that the relationship of Gap and  $E$  is not an analytic expression and care must be taken to implement this both correctly and efficiently.

The relationship between IVU21 magnetic gap and spectral peaks (equivalently  $E$ ) is both calculable from magnetic measurement data and measurable at most beamlines. Typically a beamline will make measurements that describe this relationship at a harmonic ( $n_h$ ) which is in a convenient energy range and relate this to the fundamental harmonic using the factor  $n_h$ . This relationship of gap and fundamental harmonic photon energy for IVU21 is shown in Fig. 3 for both the magnetic measurement based calculation and beamline measurement. It is this beamline measurement that is used to determine the relationship of

gap to the first harmonic energy  $E^1(gap)$  and first harmonic energy to gap  $gap(E^1)$ . Data for this relationship is loaded and stored in the IVU21 controller as sequential tabular data which is used in the forward and inverse kinematic routines for all fly moves.

The kinematic routines for this synchronous movement consist of 3 axes which must follow the same trajectory in  $E$ . For purposes of the kinematics all energies are related back to the fundamental harmonic  $E^1$  using the required user input of the desired harmonic  $n_h$ . For the Bragg angle and translation axes these are analytic and described by Eqs. (4) and (5) for the forward kinematics and Eqs. (6) and (7) for the inverse kinematics.

$$E^1(\theta) = \frac{hc}{2d_c n_h \sin(\theta + \Delta_\theta)} \quad (4)$$

$$E^1(x_c) = \frac{hc}{2d_c n_h} \left[ 1 - \left( \frac{X_{off}}{2} \frac{1}{C_X - x_c + C_T} \right)^2 \right]^{-\frac{1}{2}} \quad (5)$$

$$\theta(E^1) = \sin^{-1} \left( \frac{hc}{2d_c E^1 n_h} \right) - \Delta_\theta \quad (6)$$

$$x_c(E^1) = C_X + C_T - \frac{X_{off}}{2} \left[ 1 - \left( \frac{hc}{2d_c E^1 n_h} \right)^2 \right]^{-\frac{1}{2}} \quad (7)$$

The kinematic descriptions for gap versus energy are intuitively the curve shown in Fig. 3 however are somewhat more difficult to implement due to their non-analytic nature. It is required that this data be describable by a 1-to -1 cubic spline which then may be used for the forward and inverse kinematics. This functionality does not exist per se on the controller so the cubic spline and numerical lookup were programmed into the forward and inverse kinematics using a modified version of a standard algorithm [8]. One may be tempted to use the spline move features on this particular controller, but these pertain to programs only (not coordinate systems) and offer far less flexibility. The benefits of this method include being able to move at will to any energy, having all components synchronized in  $E$  during the motion, and doing so at a fixed velocity in  $E$ .

#### 5. Trigger

A trigger signal is generated by a PLC running on the IVU21 controller which controls a TTL output on the HDCM controller via the fiber MACRO link. The central energy, or energy of interest ( $E_i$ ) is determined by the  $E_0$  (first),  $E_f$  (last), and  $N_t$  (number of triggers) such that the  $i$ th energy is given by  $E_i = E_0 + i(E_f - E_0)/(N_t - 1)$ . The data acquisition time  $t_a$  along with the trigger width  $\sigma_E$  determine the scan speed  $v_E = \sigma_E/t_a$ . The data acquisition window surrounds symmetrically the  $E_i$  such that  $|E - E_i| < \sigma_E/2$ . The trigger generated in the PLC is on the leading edge of this window (e.g. at  $E_i \pm \sigma_E/2$  for positive and negative scan directions respectively) and is made as short as possible as only the leading edge (in time) of that signal is used and falling edge ignored.

The trigger signal output from the HDCM controller is input into a channel on a Quantum Detectors Zebra box [9] which is configured to generate a pulse of width matching the acquire time of the Xspress3 on the rising edge of the incoming trigger signal, which is output to the Xspress3 trigger input. An additional output of width 0.1 ms is configured to output on both the rising and falling edge of the aforementioned acquire signal which is used as the scaler advance signal. These trigger signals are described pictorially for ascending and descending scans in energy space in Fig. 5. In this configuration the acquisition by the Xspress3 is precisely matched in time to the scaler counts and is much less susceptible to beam deviations or top-up injection effects. Bins in the scaler which are between acquisition windows will be excluded from data analysis, but may serve some diagnostic purposes. Although a Zebra box is used it is noted that any high precision timing device which is capable of remote configuration would be a suitable alternative.

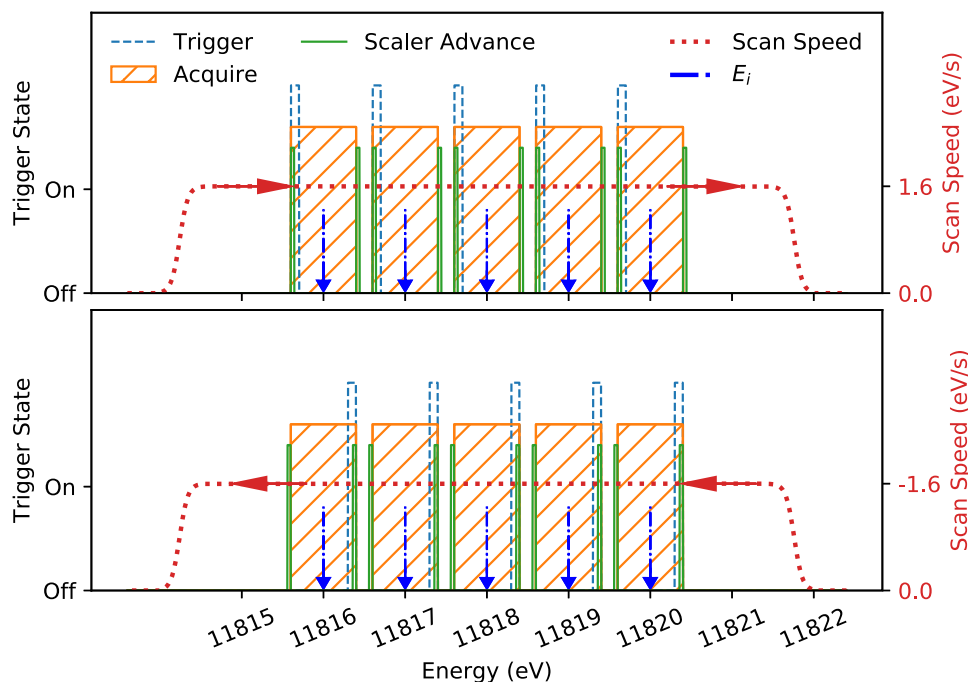


Fig. 5. Example of the trigger signal structure for fly scans ascending (top) and descending (bottom) energy scans.

The small inherent fluctuations in the leading edge of the trigger are primarily due to the frequency with which user PLCs are executed by the controller and depends on internal CPU load. In this implementation the fluctuation is only manifest in the positive time direction. When running scans this is observed to be less than 3 ms (which for example would correspond to a maximum shift of  $E_i$  per trigger of 30 meV at a scan speed of 10 eV/s). Since the acquisition high and scaler advance signals are determined to high precision in time by the Zebra box the acquisition widths and corresponding scaler counts remain unaffected in time and energy width. For measurements where this small shift in  $E_i$  may be a concern the implementation also includes a trigger timing offset input which will move the trigger in time without affecting device synchronization.

Any number of scan passes can be performed in unidirectional or bidirectional mode in one continuous scan run, either pausing at the end of each pass and waiting for an unpause signal or continuing uninterrupted. The option of pausing at the end of each pass has some utility in ease of collection of possibly very large datasets and potentially enabling more self-aware experiments if for example decisions need to be made based on statistics or even beamline adjustments are to be done by future artificial intelligence or machine learning algorithms. The results shown herein are using this pass and pause method to allow for data collection and readout from multiple sources and filesystems.

The Bluesky [10] software handles the configuration of input parameters for a scan and gathering the resultant data to be sent to the databroker. A Python class was created for the fly scan (*flyer*) using the Ophyd hardware abstraction library. The *flyer* is then used by the bluesky library to run fly scans. The *flyer* consists of four special methods: *kickoff*, *complete*, *describe\_collect*, *collect*. The *kickoff* method is used to initiate the fly scan by first setting the scanning parameters and detector parameters and finally by issuing the start scan command via the associated EPICS Process Variables (PVs). *Complete* monitors the status of the scan for completion using ophyd's status objects. The *describe\_collect* method is used to declare the layout of the data to be generated by bluesky's RunEngine. The *collect* method generates and emits the document stream containing the collected data and file references which are then saved to a Mongo database via the databroker library's application programming interface (API). The *kickoff* step is done once, and the *complete* through *collect* steps can be

repeated multiple times as needed, and the resulting data from each repetition (or a pass) is saved in a separate stream, allowing users to check individual passes via the databroker API to access the data in a tabular form or to extract corresponding images from the detector.

## 6. Results

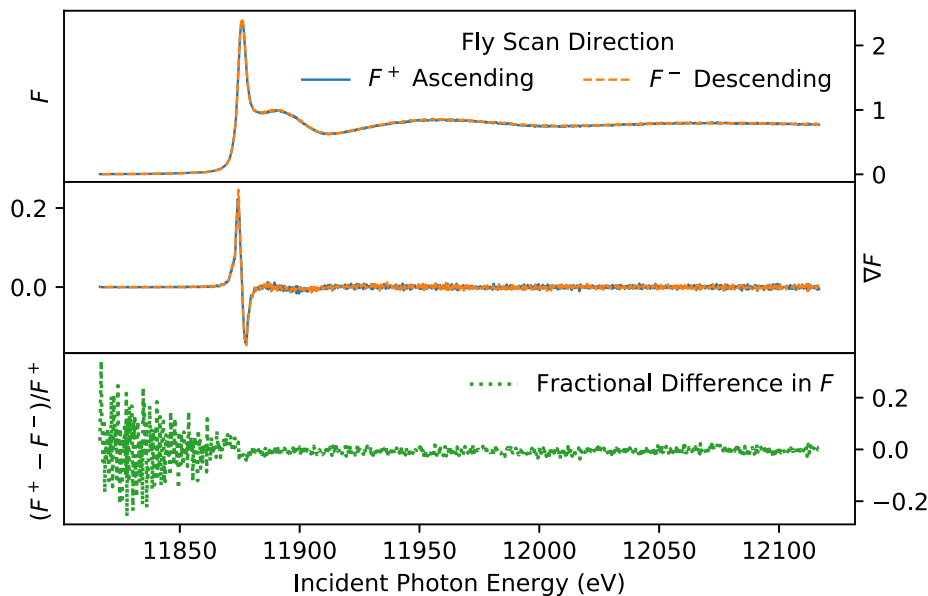
Two solutions were made for testing this new fly scan capability. One is a 2 mM Cr(VI) solution made from sodium dichromate dihydrate  $\text{Cr}_2\text{H}_4\text{Na}_2\text{O}_9$  (Alpha Aesar) and stored dark until use. The other is a 2 mM As(III) solution made from an acidified 100 mM arsenite stock solution. The stock solution was made from sodium arsenite  $\text{NaAsO}_2$  (Sigma) and acidified to 1% with HCl. Both solutions were sealed under nitrogen and stored dark until use.

Fig. 6 shows two consecutive passes of a bidirectional scan of the 2 mM As(III) sample using the 7th harmonic at a scan speed of 1.67 eV/s, 0.09 s acquire time, from 11816.7 to 12116.7 eV with a pitch of 0.25 eV and shows no directional bias in either the fluorescence spectra or the gradient. In addition to the example shown in Fig. 6 a set of 30 bidirectional scans were taken for the same sample in one run at a scan speed of 1.6 eV/s, 0.5 s acquire time, from 11816.7 to 12116.7 eV with a pitch of 1 eV. The peak in each measurement falls within the same 0.8 eV wide triggered acquire window corresponding to 11875.7 eV. The maximum gradient in these spectra is observed to be at 11874.47 eV with a standard deviation of 0.42 eV, which is smaller than the 1 eV trigger spacing.

A traditional step scan and 2 fly scans of the 2 mM As(III) sample are compared in Fig. 7 all having a measurement pitch of 1 eV. The step scan acquire time is 0.5 s and the time to completion is 10 min with the majority of the 7.5 min of overhead coming from the start and stop action of the IVU, HDCM, and all associated readout hardware. The first fly scan shown in this figure has the same acquire time and at 1.6 eV/s completes in approximately 3 min with considerably higher accuracy. The final fly scan shown in this figure corresponds to a scan speed of 10 eV/s and an acquire time of 45 ms which is completed in nearly 30 s representing a factor of 20 times reduction in scan time while maintaining very high accuracy.

Notably the step scan produces the least smooth curve among the 2 mM As(III) scans. It is perhaps easy to mistake this observation to





**Fig. 6.** Fluorescence spectra collected using the fly scan method for 2 mM As(III) in the ascending ( $F^+$ ) and descending ( $F^-$ ) incident photon energy directions in the energy range from 11816.7 to 12116.7 eV with a trigger pitch of 0.25 eV.  $\bar{F}_{diff} < 2.5 \times 10^{-3}$  where  $1/\sqrt{N_t} = 28.9 \times 10^{-3}$ .

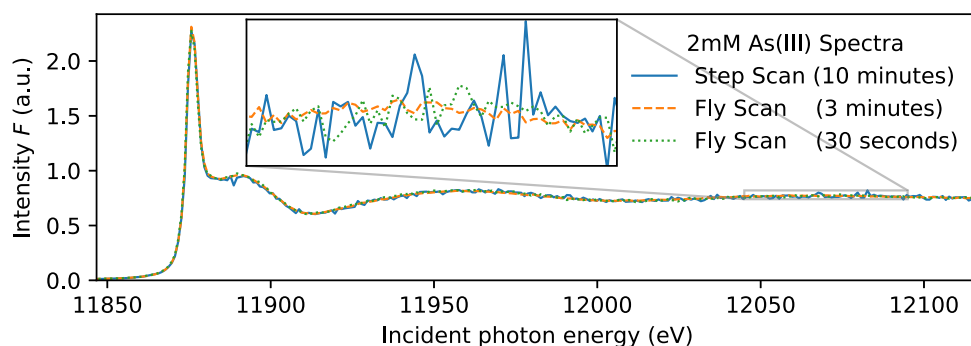


**Fig. 7.** Step scan compared to two fly scans, the first of which has the same acquire time completing in less than one third the time and the second completing in approximately 5% of the time taken for a step scan and retaining higher accuracy.

low statistics or electron beam motion, however this cannot be the case as the first fly scan is statistically similar having the same acquire window and both fly scans show very good behavior in this respect. The behavior is not attributable to the IVU21 motion both because of the very small steps in magnetic gap and that the peak of the spectrum is wide relative to the energy pitch and flat at the top. The most likely cause of this is the stop-start nature of the step scan and that the HDCM alignment in the stopped state is less accurate than while in motion, which is not uncommon for many motion systems. Comparing this step scan to the average of an independent set of 25 fly scan measurements (1.6 eV/s with 0.5 s acquire time) in the signal region above 12 keV gives an average signal to noise ratio of 56:1. The same comparison for the equivalent fly scan yields a signal to noise of 180:1, while the scan at 10 eV/s yields 95:1.

An example of one scan of the 2 mM Cr(VI) sample in a lower energy range and using the 3rd harmonic as compared to the 2 mM As(III) scans is shown in Fig. 8. Several features are noted in this figure including the pre-peak and maximum gradient above 5995 eV. In a series of 65 consecutive bidirectional scans at 1 eV/s with an acquire time of 0.9 s and pitch of 1 eV in the energy range of 5964 eV to 6139 eV the pre-peak always falls in the same 0.9 eV acquire window at 5993 eV. The maximum gradient above 5995 eV (the edge) in these scans is determined to be  $6002.44 \pm 0.50$  eV. The scan ranges for scans of both the 2 mM As(III) and 2 mM Cr(VI) samples are indicated on the respective harmonic curves in Fig. 1.

The fluorescence spectra shown are only the Xpress3 detector channel summations divided by the ion chamber counts gathered by the scaler. It is important to note that in the analysis of this data no additional normalization has been performed in neither the analysis nor the plots shown herein.

## 7. Conclusions

A method for high precision real-time insertion device and monochromator synchronization and hardware triggered fly scanning has been implemented for the SRX beamline at NSLS-II. The fly scan method has been shown to be significantly faster and more accurate than the previous step scan method. In the 2 mM Cr(VI) and 2 mM As(III) samples investigated scan times were reduced by up to a factor of 20 and have shown less fluctuations during scans than their step scan equivalents. Several future implementations of this synchronized fly scan method are currently underway for other beamlines at NSLS-II, including for soft x-ray beamlines utilizing undulators or elliptically polarizing undulators.

## CRediT authorship contribution statement

**D. Hidas:** Conceptualization, Methodology, Software, Validation, Formal analysis, Investigation, Resources, Data curation, Writing – original draft, Writing – review & editing, Visualization, Supervision,

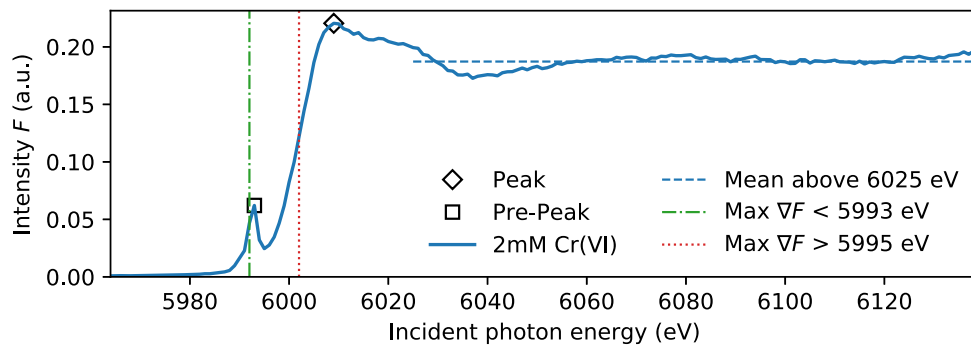


Fig. 8. Example fly scan for the 2 mM Cr(VI) sample highlighting the peak, pre-peak, maximum gradient, and other parameters of interest.

Project administration. **A.M. Kiss:** Methodology, Software, Validation, Investigation, Resources, Data curation, Writing – review & editing, Supervision. **M. Rakitin:** Software, Validation, Investigation, Writing – review & editing. **J. Sinsheimer:** Validation, Resources, Writing – review & editing. **T. Tanabe:** Resources, Project administration. **M. Musardo:** Resources.

#### Declaration of competing interest

The authors declare that they have no known competing financial interests or personal relationships that could have appeared to influence the work reported in this paper.

#### Acknowledgments

The authors would like to thank and acknowledge Sarah Nicholas from the XFM beamline at the NSLS-II for preparing the standard solutions for measurement. This research used resources from the SRX beamline of the National Synchrotron Light Source II, a U.S. Department of Energy (DOE) Office of Science User Facility operated for the DOE Office of Science by Brookhaven National Laboratory under Contract No. DE-SC0012704.

#### References

- [1] D. Hidas, Computation of synchrotron radiation on arbitrary geometries in 3D with modern GPU, multi-core, and grid computing, in: Proceedings, 8th International Particle Accelerator Conference, IPAC 2017, Copenhagen, Denmark, May 14–19, 2017, 2017, WEPIK121, <http://dx.doi.org/10.18429/JACoW-IPAC2017-WEPIK121>.
- [2] M. Musardo, D. Harder, C. Kitegi, T. Tanabe, Magnetic measurements of the NSLS-II insertion devices, in: Proceedings, 6th International Particle Accelerator Conference, IPAC 2015, Richmond, Virginia, USA, May 3–8, 2015, 2015, TUPJE037, <http://dx.doi.org/10.18429/JACoW-IPAC2015-TUPJE037>.
- [3] O. Chubar, C. Kitegi, Y.-C. Chen-Wiegart, D. Hidas, Y. Hidaka, T. Tanabe, G. Williams, J. Thieme, T. Caswell, M. Rakitin, L. Wiegart, A. Fluerasu, L. Yang, S. Chodankar, M. Zhernenkov, Spectrum-based alignment of in-vacuum undulators in a low-emittance storage ring, *Synchrotron Radiat. News* 31 (2018) 4–8, <http://dx.doi.org/10.1080/08940886.2018.1460173>.
- [4] J. Krempaský, U. Flechsig, D. Korhonen, D. Zimoch, C. Quitmann, F. Nolting, Synchronized monochromator and insertion device energy scans at SLS, *AIP Conf. Proc.* 1234 (1) (2010) 705–708, <http://dx.doi.org/10.1063/1.3463307>, arXiv: <https://aip.scitation.org/doi/pdf/10.1063/1.3463307>. URL <https://aip.scitation.org/doi/abs/10.1063/1.3463307>.
- [5] D. Hidas, et al., Precision insertion device control and simultaneous monochromator fly scanning for NSLS-II, in: 3rd North American Particle Accelerator Conference, NAPAC2019, 2019, TUPLS09, <http://dx.doi.org/10.18429/JACoW-NAPAC2019-TUPLS09>.
- [6] Y.-c.K. Chen-Wiegart, G. Williams, C. Zhao, H. Jiang, L. Li, M. Demkowicz, M. Seita, M. Short, S. Ferry, T. Wada, H. Kato, K.W. Chou, S. Petrash, J. Catalano, Y. Yao, A. Murphy, N. Zumbulyadis, S.A. Centeno, C. Dybowski, J. Thieme, Early science commissioning results of the sub-micron resolution X-ray spectroscopy beamline (SRX) in the field of materials science and engineering, *AIP Conf. Proc.* 1764 (1) (2016) 030004, <http://dx.doi.org/10.1063/1.4961138>, arXiv: <https://aip.scitation.org/doi/pdf/10.1063/1.4961138>. URL <https://aip.scitation.org/doi/abs/10.1063/1.4961138>.
- [7] L.R. Dalesio, J.O. Hill, M. Kraimer, S. Lewis, D. Murray, S. Hunt, W. Watson, M. Clausen, J. Dalesio, The experimental physics and industrial control system architecture: past, present, and future, *Nucl. Instrum. Methods Phys. Res. A* 352 (1) (1994) 179–184, [http://dx.doi.org/10.1016/0168-9002\(94\)91493-1](http://dx.doi.org/10.1016/0168-9002(94)91493-1), URL <https://www.sciencedirect.com/science/article/pii/0168900294914931>.
- [8] W.H. Press, S.A. Teukolsky, W.T. Vetterling, B.P. Flannery, *Numerical Recipes in C*, second ed., Cambridge University Press, Cambridge, USA, 1992.
- [9] T.M. Cobb, Y.S. Chernousko, I.S. Uzun, ZEBRA: a flexible solution for controlling scanning experiments, in: Proc. 14th Int. Conf. on Accelerator and Large Experimental Physics Control Systems, ICALEPCS'13, JACoW Publishing, 2013, pp. 736–739.
- [10] D. Allan, T. Caswell, S. Campbell, M. Rakitin, Bluesky's ahead: A multi-facility collaboration for an a la carte software project for data acquisition and management, *Synchrotron Radiat. News* 32 (3) (2019) 19–22, <http://dx.doi.org/10.1080/08940886.2019.1608121>, arXiv: <https://doi.org/10.1080/08940886.2019.1608121>.